Astronomy & Astrophysics manuscript no. phaethon_2016
May 18, 2016

Orbital, spin state and thermophysical characterization of near-Earth asteroid (3200) Phaethon

J. Hanuš[1,2*], M. Delbo'[2], D. Vokrouhlický[3], P. Pravec[4], J.P. Emery[5], V. Alí-Lagoa[2], B. Bolin[2], M. Devogèle[6,2], R. Dyvig[7], A. Galád[8], R. Jedicke[9], L. Kornoš[8], P. Kušnirák[4], J. Licandro[10,11], V. Reddy[12], J-P. Rivet[2], J. Világi[8], and B.D. Warner[13]

[1] Centre National d'Études Spatiales, 2 place Maurice Quentin, 75039 Paris cedex 01, France
*e-mail: hanus.home@gmail.com
[2] Laboratoire Lagrange, UMR7293, Université de la Côte d'Azur, CNRS, Observatoire de la Côte d'Azur, Blvd de l'Observatoire, CS 34229, 06304 Nice cedex 04, France
[3] Astronomical Institute, Faculty of Mathematics and Physics, Charles University, V Holešovičkách 2, 180 00 Prague, Czech Republic
[4] Astronomical Institute, Academy of Sciences of the Czech Republic, Fričova 1, CZ-25165 Ondřejov, Czech Republic
[5] Earth and Planetary Science Department, Planetary Geosciences Institute, University of Tennessee, Knoxville, TN 37996, United States
[6] Département d'Astrophysique, Géophysique et Océanographie, Université de Liège, Allèe du Six Août 17, 4000 Liège, Belgium
[7] Badlands Observatory, 12 Ash Street, P.O. Box 37, Quinn, SD 57775, USA
[8] Modra Observatory, Department of Astronomy, Physics of the Earth, and Meteorology, FMPI UK, Bratislava SK-84248, Slovakia
[9] Institute for Astronomy, University of Hawaii at Manoa, Honolulu, HI 96822, USA
[10] Instituto de Astrofísica de Canarias (IAC), CVía Láctea s/n, 38205 La Laguna, Spain
[11] Departamento de Astrofísica, Universidad de La Laguna, 38206 La Laguna, Tenerife, Spain
[12] Planetary Science Institute, 1700 East Fort Lowell Road, Tucson, AZ 85719, USA
[13] 446 Sycamore Ave., Eaton, CO 80615, USA

Received x-x-2016 / Accepted x-x-2016

ABSTRACT

Context. The near-Earth asteroid (3200) Phaethon is an intriguing object: its perihelion is only at 0.14 au and is associated with the Geminid meteor stream.

Aims. We aim to use all available disk-integrated optical data to derive reliable convex shape model of Phaethon. By interpreting the available space- and ground-based thermal infrared data and Spitzer spectra using a thermophysical model, we also aim to further constrain its size, thermal inertia, and visible geometric albedo.

Methods. We apply the convex inversion method to the new optical data obtained by six instruments together with the already existing observations. The convex shape model is then used as an input for the thermophysical modeling. We also study the long-term stability of Phaethon's orbit and spin axis by a numerical orbital and rotation-state integrator.

Results. We present a new convex shape model and rotational state of Phaethon – sidereal rotation period of 3.603958(2) h and ecliptic coordinates of the preferred pole orientation of (319°, −39°) with a 5° uncertainty. Moreover, we derive its size (D=5.1±0.2 km), thermal inertia (Γ=600±200 J m^{-2}s$^{-1/2}$K^{-1}), geometric visible albedo (p_V=0.122±0.008), and estimate the macroscopic surface roughness. We also find that the Sun illumination at the perihelion passage during past thousands of years is not connected to a specific area on the surface implying non-preferential heating.

Key words. minor planets, asteroids: (3200) Phaethon – techniques: photometric – methods: observational – methods: numerical

1. Introduction

The extraordinary near-Earth asteroid (3200) Phaethon (hereafter simply Phaethon), which currently has a perihelion distance of only 0.14 au, regularly experiences surface temperatures of more than 1 000 K. This B-type object is one of the best studied low-perihelion asteroids (Campins et al. 2009).

Phaethon has been dynamically associated to the Geminid meteor stream (Gustafson 1989; Williams & Wu 1993; Jenniskens 2006, and references therein), one of the most prominent annually periodic meteor streams. For this reason, activity around Phaethon has been searched. However, detecting the activity has always been challenging, in particular near perihelion, due to its close approaches to the Sun. Jewitt & Li (2010) and Li & Jewitt (2013) succeeded using STEREO (a solar observatory) spacecraft data from 2009 and 2011 to measure near-Sun brightening of Phaethon by a factor of two, associated with dust particles of an effective diameter ∼1 μm ejected from the surface. On the other hand, there is no evidence of gas release (Chamberlin et al. 1996). However, the observed dust produced during the perihelion passage (mass of ∼3×10^5 kg, Jewitt et al. 2013) is small compared to the mass of the whole Geminid stream (mass of ∼10^{12}–10^{13} kg, Jenniskens 1994). Moreover, these small particles are quickly swept away by the solar radiation pressure and can be hardly reconciled with the age of the Geminids. The Geminid stream consists of much larger particles than those estimated from the STEREO data with sizes from 10 μm up to about 4–4.5 cm (Arendt 2014; Yanagisawa et al. 2008), some of them might even survive the passage through the Earth's atmosphere

(Madiedo et al. 2013), and drop meteorites that have never been collected. The mechanism(s) of mass loss from Phaethon, capable to produce the massive swarm of the Geminids, is not fully understood (Jewitt et al. 2015). So far, the most convincing process consists of thermal disintegration of the surface of the asteroid (e.g, Delbo' et al. 2014) assisted by rotation and radiation pressure sweeping, or thermal desiccation cracking, or both (see the review of Jewitt et al. 2015). However, to reliably explain the total mass of the Geminid stream in the scope of its expected dispersion age of $\sim 10^3$ years (Ohtsuka et al. 2006), additional theoretical and laboratory constraints of the thermal fracture mechanism, as well as physical and surface properties of Phaethon are necessary.

Concerning the physical properties of Phaethon, Licandro et al. (2007) found that spectral shape of Phaethon is similar to that of aqueously altered CI/CM meteorites and of hydrated minerals. However, it is not clear whether the heating is happening due to the close approaches with the Sun or in Phaethon's parent body (or both). The large main-belt asteroid (2) Pallas has been identified (de León et al. 2010), from spectroscopic and dynamical arguments, as the source of Phaethon. However, the spectrum of Phaethon is generally bluer than that of Pallas. Whether this spectral slope difference is due to the extreme solar-heating on the former, compared to the latter, or to different grain size of the regolith of these bodies is still not clear (de León et al. 2010). In the case of a spin state with obliquity of $\sim 90°$ (Krugly et al. 2002; Ansdell et al. 2014), one of the hemispheres of Phaethon would receive substantially more solar heating during the perihelion passage as it is always facing the Sun. But Ohtsuka et al. (2009) report no significant spectral variability across the body, which could indicate that, contrary to expectations (Hiroi et al. 1996), the sun-driven heating does not affect the spectral properties, or that Phaethon was not always exposing the same hemisphere at perihelion, or a combination of both. Interestingly, the composition of Pallas, deduced from spectroscopic data near three microns, matches those of heated CM chondrites and is also similar to that of the CR chondrite Renazzo (Sato et al. 1997). This is due to the presence of the spectroscopic signature of phylosilicates. Even more interestingly, Madiedo et al. (2013) also indicate that the composition of the Geminids, deduced from spectra of atmospheric flashes, is consistent with those of CM chondrites. On the other hand, a good match of Phaethon's near IR spectra with those of CK chondrites was also found (Clark et al. 2010).

Concerning the orbital evolution of Phaethon, we note that Chernetenko (2010), and also Galushina et al. (2015), report to have detected a transverse acceleration component in Phaethon's heliocentric motion. In fact, Vokrouhlický et al. (2015) obtained a similar result, but their uncertainty was larger than that of Chernetenko (2010), such that the signal-to-noise ratio was only about $\simeq$ 1.4, and for that reason the value was not listed in their Table 1 (we do not know the reason for the difference). We have made use of our pole solutions from Sec. 4.1 and verified that the magnitude of the transverse acceleration reported by Chernetenko (2010) is compatible with prediction of the Yarkovsky effect, assuming low bulk density $\simeq 1$ g cm^{-3} and thermal inertia $\simeq 600$ J m^{-2}s$^{-1/2}$K^{-1}or slightly smaller (Sec. 4.2). Alternately, the recoil effects of outgassing and particle ejection near perihelion may also contribute to the effective transverse orbital acceleration. Galushina et al. (2015), however, estimate that the Yarkovsky effect should be about an order of magnitude larger. In any case, the current situation suggests that we are on the brink of the Yarkovsky effect determination for Phaethon and it is very reasonable to expect that it will be fairly well constrained during its upcoming close encounter in December 2017 (especially, if radar astrometry will be obtained). Moreover, Gaia astrometry will also significantly help to constrain the Yarkovsky effect. While certainly more photometric and thermal observations will be taken in the late 2017, it would be interesting to collect the current state-of-the-art knowledge about Phaethon's physical parameters relevant for the Yarkovsky effect determination (such as the size, albedo, thermal inertia, spin axis direction, macroscopic shape, and surface roughness). If a rich-enough dataset is available, the Yarkovsky effect allows determination of the asteroid bulk density: see Vokrouhlický et al. (2015) for general overview, and Chesley et al. (2014), Emery et al. (2014), and Rozitis et al. (2013); Rozitis et al. (2014); Rozitis & Green (2014) for specific cases. Note that knowing the bulk density of asteroids is fundamental to shed light on their internal structure (such as monolithic vs rubble-pile). For example, when compared with the densities of meteorites, one can deduce the porosity of asteroid interiors. These physical properties of asteroids reflect the accretional and collisional environment of the early solar system.

The spin state of Phaethon was first constrained by Krugly et al. (2002): they derived two pole solutions with low ecliptic latitude (about –10 deg). Recent work of Ansdell et al. (2014) based on additional photometric data reports a single pole solution compatible with one of the pole solutions of Krugly et al. (2002) and provide a convex shape. Their shape model is based on disk-integrated optical data and computed by the convex inversion method (Kaasalainen & Torppa 2001; Kaasalainen et al. 2001). However, from their Fig. 3, it is obvious that the rotation period is not unique and their reported interval includes several local minima that correspond, in principle, to different pole solutions (evident in their Figs. 4 and 5). We are thus convinced that the shape model needs additional attention before using it in further applications. Thus, we refine the shape model by using new optical data.

Thermal inertia Γ, size D, Bond albedo A, and surface roughness can be derived by using a thermophysical model (hereafter TPM, Lagerros 1996, 1997, 1998) to analyze thermal infrared data (see, e.g., Delbo' et al. 2015, for a review). Although thermal infrared data of Phaethon, which allowed determination of a radiometric diameter of Phaethon, exist (Green et al. 1985; Tedesco et al. 2002; Usui et al. 2011, 2013), there is currently no estimation of the value of the thermal inertia for this body.

In Sect. 2, we describe optical data that we used for the shape modeling, and thermal infrared data and Spitzer spectra that made the thermophysical modeling possible. Lightcurve inversion and TPM methods are presented in Sect. 3. We derive a convex shape model of Phaethon in Sect. 4.1 and use it in the TPM in Sect. 4.2. The orbital and spin axis evolution is discussed in Sect. 4.3. Finally, we conclude our work in Sect. 5.

2. Data

2.1. Optical disk-integrated photometry

We gather a total of 55 dense-in-time lightcurves of Phaethon spanning 1994–2015, including 15 lightcurves from Ansdell et al. (2014), 3 lightcurves from Pravec et al. (1998), one lightcurve from Wisniewski et al. (1997) and 7 lightcurves from Warner (2015). In addition, we obtained 29 new lightcurves with six different instruments. All lightcurves are summarized in Tab. 1.

All lightcurves are based on aperture photometry in standard filter systems, either differential or absolute. The images were bias- and flat-field corrected usually using sky flats. As the data were obtained by different telescopes and by a large number of observers, the photometry reduction procedures may slightly vary, but all follow the standard procedures. Some of the data were initially absolutely calibrated, but we normalized them like all remaining lightcurves. Only the relative change of the brightness due to rotation and orientation with respect to the Sun and the observer is necessary for the lightcurve inversion. Moreover, the epochs were light-time corrected.

We obtained 4 lightcurves of Phaethon with the University of Hawaii 2.2-meter telescope (UH88) located near the summit of Maunakea in Hawaii between August and October 2015. We used the Tektronix 2048x2048 CCD camera that has a 7.5′x7.5′ field of view corresponding to a pixel scale of 0.22″. The images obtained were nyquist-sampled corresponding to the typical seeing of ∼ 0.8′ during the observations and to reduce readout time. Exposures were between 120–180 s in the Sloan r' filter. Non-sideral tracking at half the rate of Phaethon was used so the PSFs of the asteroid and background stars have similar morphologies. The lightcurves taken with the UH88 are semi-dense with 15-25 minutes between observations and have sufficient density because the rotation period of Phaethon is 3.6 h. Semi-dense lightcurves were obtained to allow the simultaneous observations of additional targets.

We also used the C2PU (Centre Pédagogique Planète et Univers) 1.04 meter telescope situated in the Calern observing station of Observatoire de le Côte d'Azur in France (06° 55' 22.94" E, 43° 45' 13.38" N, 1270 m, IAU code 010). This telescope has a f/3.2 prime focus with a three-lenses Wynne corrector and a QSI632 CCD Camera with a built-in filter wheel. We obtained 7 lightcurves between December 2014 and February 2015.

Four lightcurves from 2004 and 2007 were obtained at Modra observatory in Slovakia (Galád et al. 2007). Open filter and standard aperture photometry were used.

We used 66 cm f/4.8 Newtonian telescope at Badlands Observatory, Quinn, South Dakota, to observe Phaethon over the course of two weeks ending on December 12, 2004. The data were obtained using an Apogee 1Kx1K CCD camera with SiTe detector. After basic calibration, the data were reduced using Canopus (Warner 2006).

Data from apparitions in 1994, 2003 and 2004 consisting of 8 lightcurves were obtained by the 65 cm telescope in Ondřejov, Czech Republic. In all cases, Cousins R filter and aperture photometry were used. Moreover, data from 2004 were absolutely calibrated in the Cousins R system with Landolt (1992) standard stars with absolute errors of 0.01 mag.

Four lightcurves from the apparition in 1998 were obtained with the 82cm IAC-80 Telescope at Teide Observatory (Canary Islands, Spain) using a broadband Kron-Cousins R filter. We used standard aperture photometric procedures and did absolute photometry using at least 3 Landolt field stars (Landolt 1992). The exposure time was 300 seconds during all nights and due to the trailed stars, only absolute photometry was possible. A Thomson 1024×1024 CCD chip was used, offering a field of nearly 7.5 arcmin.

The data from UH88 and Ondřejov were reduced with our custom made aperture photometry software Aphot+Redlink developed by Petr Pravec and Miroslav Velen.

Our lightcurves in the standard format used for the lightcurve inversion (i.e., epochs and brightness are accompanied by ecliptic coordinates of the Sun and Earth centered on the asteroid)

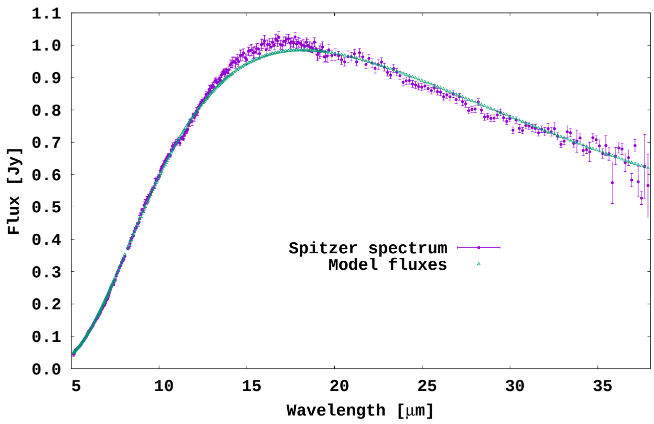

Fig. 1. The Spitzer IRS spectral data of Phaethon from January 14, 2005. We show the observed spectra and the best-fitting TPM model for the first pole solution (D = 5.1 km, p_V = 0.122, Γ = 600 J m^{-2}s$^{-1/2}$K^{-1}, high macroscopic roughness).

are available in the Database of Asteroid Models from Inversion Techniques (DAMIT[1], Ďurech et al. 2010).

2.2. Thermal infrared data

Measurements of asteroids in thermal (mid-) infrared are, in general, difficult to obtain, thus it is not surprising that there are only few past measurements available for Phaethon. The IRAS satellite observed Phaethon in 1983 in four filters providing a total of 19 individual measurements at 6 epochs (see Tab. 2). We extracted IRAS space-based observations of Phaethon from the SIMPS database of Tedesco et al. (2002). Each epoch consists of thermal infrared data in filters with isophotal wavelengths at 12, 25 and 60 μm. Moreover, one epoch contains flux at 100 μm as well. These data were already analyzed by the means of a standard thermal model: radiometric diameter of 5.1 ± 0.2 km and geometric visible albedo of 0.11 ± 0.01 were derived by Tedesco et al. (2004).

We also extracted ground-based observations presented by Green et al. (1985), which resulted in 12 measurements at 9 different wavelengths. Note that we excluded fluxes at wavelengths smaller than 4 μm, which were contaminated by the reflected light component, and transformed fluxes into Jansky units (Tab. 2). The authors reported radiometric diameter of 4.7 ± 0.5 km and geometric visible albedo of 0.11 ± 0.02.

The AKARI satellite (Ishihara et al. 2010) observed Phaethon as well. Unfortunately, the fluxes are not publicly available. Radiometric diameter (4.17 ± 0.13 km) and geometric visible albedo (0.16 ± 0.01) were reported by Usui et al. (2011).

These reported radiometric sizes are not fully compatible with each other. The differences are likely caused by the underestimation of model systematics (thus reported errorbars are too small) and possible calibration errors.

Observations by the Spitzer InfraRed Spectrograph (IRS Houck et al. 2004) started at 22:14:54 on 14 January 2005 (UT) and ended at about 22:24:30 UT on the same day. This spectrum covers mid-infrared wavelengths of 5–37 μm (Fig. 1). The Spitzer order-to-order flux uncertainties are 10% or lower (Decin et al. 2004). We measured 4 orders and used an overall relative scaling for the final flux. We consider those as four indepen-

[1] http://astro.troja.mff.cuni.cz/projects/asteroids3D

dent absolute flux measurements, so we always treat the final flux uncertainty as 5%, which should translate to 2.5% in diameter. Typically, sizes derived by the thermophysical model have uncertainties about 5% or higher, thus the calibration uncertainty does not affect the final size uncertainties significantly when added in quadrature.

3. Methods

3.1. Lightcurve inversion method

As the usually non-spherical asteroids rotate around their rotational axis, they change the illuminated part of their bodies with respect to the observer, and thus exhibit temporal variations of their brightness. The lightcurve inversion methods (LI) aim, under various assumptions, to search for unknown parameters (including sidereal rotation period, spin axis orientation, and shape) that affect the observed brightness. The most commonly used inversion method, which assumes a convex shape model, is the convex inversion of Kaasalainen & Torppa (2001); Kaasalainen et al. (2001).

We systematically run this gradient-based LI method with different initial periods and pole orientations to sample the parameter space. A fine enough grid of initial parameter values guarantees that we do not omit any local minimum. If the photometric dataset is rich in observing geometries, i.e., we sample all sides of the asteroid, we ideally derive one combination of parameters, i.e., a solution, that fits the observed data significantly better than all the other combinations (by means of a chi-square metric). To be more precise, we use a gradient-based method with the Levenberg-Marquardt implementation that converges to the closest minimum for a set of initial parameter values. We aim to find the global minimum in the parameter space by investigating all possible local minima. Moreover, our applied method assumes that the asteroid rotates along its principal axis with a maximum momentum of inertia. We always check if this condition is fulfilled for our final shape model.

3.2. Thermophysical model

A TPM calculates thermal infrared fluxes for a given set of physical parameters, illumination and observing geometry of an asteroid. Classically, the shape and the rotational state of the asteroid are considered as fixed inputs for the TPM. Such TPM has been applied, for example, to shapes of asteroids (341843) 2008 EV_5 and (101955) Bennu based on radar imaging (Alí-Lagoa et al. 2014; Emery et al. 2014), and to convex shapes from optical data of asteroids (25143) Itokawa and (1620) Geographos (Müller et al. 2014; Rozitis & Green 2014). The downside of this approach is that it does not account for the uncertainties in the shape model and the rotation state. However, there is growing evidence that these uncertainties are affecting the TPM results (Rozitis & Green 2014; Hanuš et al. 2015). The recent TPM approach of Hanuš et al. (2015), called the varied-shape TPM, is based on mapping the shape and rotation state uncertainties by generating various shape models of an asteroid from its bootstrapped optical data. These shape models are then used as inputs for the "classical" TPM scheme.

TPM solves the heat-conduction equation over the relevant top surface layer of an airless body and computes temperatures for each surface element, usually a triangular facet. Thermal fluxes in desired wavelengths and directions can be then easily outputed as well. In our work, we use a TPM implementation of Delbo' et al. (2007) and Delbo' (2004) that is based on

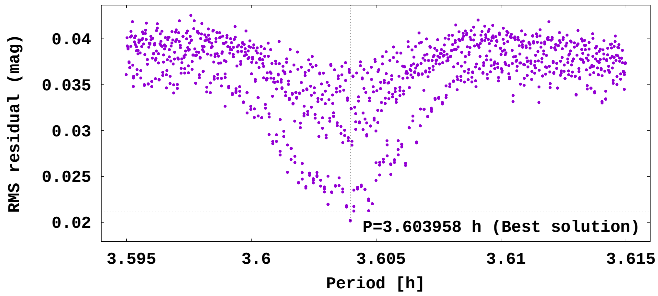

Fig. 2. Lightcurve inversion search for the sidereal rotation period of Phaethon: each point represents a local minimum in the parameter space (i.e., rotation period, pole orientation, shape). The point with the lowest rms is the global minimum and the horizontal line indicates a value with a 10% higher χ^2 than the best-fitting solution.

TPM developement by Lagerros (1996, 1997, 1998), Spencer et al. (1989), Spencer (1990), and Emery et al. (1998). This thermophysical model, recently used in Alí-Lagoa et al. (2014) and Hanuš et al. (2015), takes an asteroid's shape model, its rotation state, and a number of physical parameters such as Bond albedo A, macroscopic surface roughness, and thermal inertia Γ as input parameters. The macroscopic roughness is parametrized by an opening angle and areal density of a spherical crater on each surface element. This crater is divided into several, typically 40, surface elements, and a heat-conduction equation, accounting for shadowing and mutual heating, is solved in each one of these elements. We used five different combinations of the opening angle and areal density in the TPM and consider zero (opening angle=0°, areal density=0), low (30°, 0.3), medium (50°, 0.5), high (70°, 0.7) and extreme (90°, 0.9) roughness. Knowledge of absolute magnitude H and slope G is required as well.

By running TPM with different values of input parameters, and subsequently, by comparing computed fluxes with observed ones, we can constrain some/all of these parameters. Typically, we minimize the metric

$$\chi^2 = \sum_i \frac{(s^2 F_i - f_i)^2}{\sigma_i^2}, \quad (1)$$

where f_i are the observed fluxes, $s^2 F_i$ the modeled fluxes, where the scale factor s corresponds to the asteroid size, and σ_i represent the errors of fluxes f_i, where i samples all individual measurements.

4. Results and Discussions

4.1. Shape model and rotation state

Optical dense data suggest a small lightcurve amplitude of ~0.1–0.15 magnitude, which is comparable with the typical noise of the available sparse-in-time measurements from astrometric surveys (Hanuš et al. 2011; Ďurech et al. 2016). This implies that the sparse-in-time data should be dominated by noise. On the other hand, we have a large number of dense lightcurves from many apparitions, which should be sufficient for a successful shape model determination, thus we decided to use only those data. However, we excluded three lightcurves from our analysis due to their higher photometric noise (see Tab. 1). Moreover, we also did not use the lightcurve from Wisniewski et al. (1997)

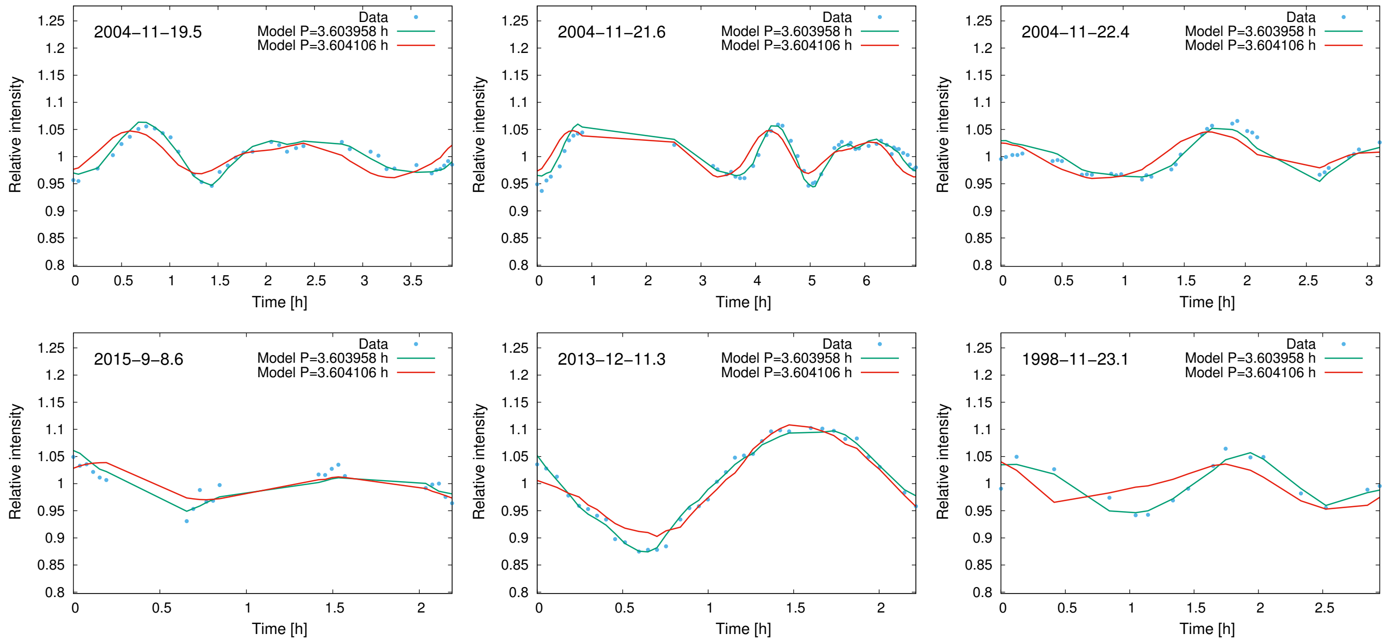

Fig. 3. Comparison between fits of several lightcurves that correspond to the best (green lines) and the second best (red lines) periods. The real measurements are plotted with blue dots.

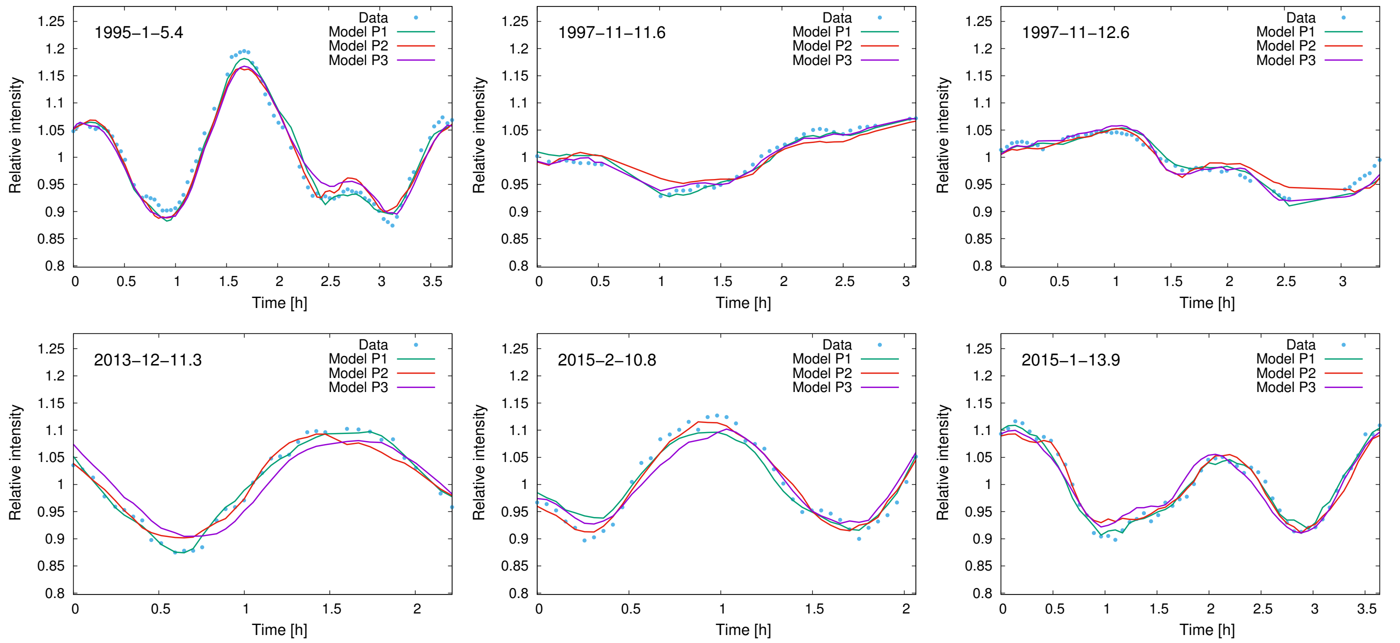

Fig. 4. Comparison between fits of several lightcurves that correspond to the best (P1, green lines), the second best (P2, red lines), and the third best (P3, purple lines) pole solution. The real measurements are plotted with blue dots.

for the final shape model determination, because it was not in an agreement with our best-fitting model, namely we obtained a significant offset of about 20 minutes in the rotation phase. Although we did not find any inconsistency in the original dataset of Wisniewski et al. (1997), the error in the lightcurve cannot be fully ruled out. Other possible explanations involve, for example, effects of concavities or period change due to activity during 1989–1994 apparitions. However, our photometric dataset does not allow us to make reliable conclusions.

The fit in the rotation period sub-space (we sampled periods in the proximity of the expected value that is well defined by the lightcurve observations) exhibits one prominent minimum that corresponds to the period of $P = 3.603958$ h (see Fig. 2). The corresponding χ^2 is by more than 10% smaller than those for all other periods, which is, according to our experience, sufficient to exclude all other solutions. Nevertheless, we show in Fig. 3 the comparison between fits of several lightcurves that correspond to the best and the second best periods. Next, we densely sam-

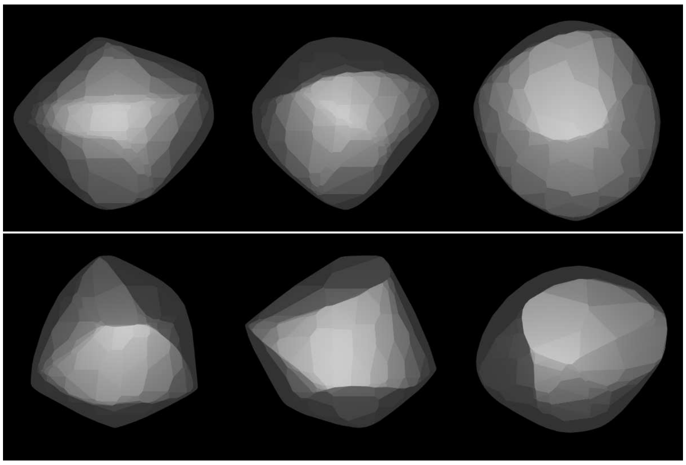

Fig. 5. Shape models that correspond to the first (top, λ=319°) and second (bottom, λ=84°) pole solutions derived from dense data only. Each panel shows the shape model at three different viewing geometries: the first two are equator-on views rotated by 90°, the third one is a pole-on view.

pled various initial pole orientations: we ran the convex inversion with the best-fitting period and all the initial pole guesses. We obtained two pole solutions that fit the optical data significantly better than all the others. The first solution provides a slightly better fit than the second one, thus the former is favored (the difference in chi-square is only about 5%). Nevertheless, we still consider the second solution below, since it is a plausible solution. The remaining pole solutions have χ^2-values more than 15% higher, thus could be excluded. We show the comparison between fits of several lightcurves that correspond to the first, second and third best poles in Fig. 4. The resulting rotation state parameters are listed in Tab. 3 and the three-dimensional shapes at different viewing geometries are shown in Fig. 5. The uncertainties in the pole direction, estimated by analyzing dispersion of 30 solutions based on bootstrapped photometric data sets, are both of ~5°.

We have two poles with ecliptic latitude β of about –39° and different ecliptic longitudes λ (319°, and 84°). Moreover, their shapes seem to be different, thus these solutions cannot be considered as mirror. The presence of two pole solutions is most likely caused by the high number of lightcurves with low amplitude, high noise, low period sampling, short timespan, and by an observational effect (not enough distinct viewing geometries).

The shape solution of Ansdell et al. (2014) (P=3.6032±0.0008 h, λ=85±13°, β=–20±10°, see also Tab. 3) is close to our second pole solution, but matches only considering the extreme values of the parameter uncertainties. Our period estimate has significantly higher precision, because we found a global minimum in the period space. Ansdell's interval of periods includes multiple local minima (see their Fig. 3), thus we cannot speak about a unique solution in their case. In principle, for each local minimum, there exists a best pole solution that does not necessarily need to be the same within different local minima. The correct approach would be to check all the possible pole solutions for each initial period (local minimum) and hope for only a few pole solutions to repeat. Ansdell et al. performed a statistical approach, where they determined the best-fitting period and associated error using a Monte Carlo technique. They added random Gaussian-distributed noise scaled to typical photometry errors of ~0.01 mag to each light curve point and they modified the photometric data multiple times by generating each data point from a random distribution around its observed value taking the photometric uncertainties as dispersions. The main caveat is that this approach only takes the best-fitting period value, thus does not necessarily sample all local minima. As a natural consequence, some of the acceptable solutions could be easily missed. Ansdell et al. created a histogram of pole solutions that were derived based on different modified datasets and chose the most frequent solution. However, it is clear from their Figs. 4 and 5 that other pole solutions (e.g., those with λ ~320°) have rms comparable with their best solution. Our conclusion is that the photometric dataset used in Ansdell et al. (2014) was not sufficient for a unique shape model determination, and the reported pole is only one out of many possible solutions.

Our spin solution does not match the one of Krugly et al. (2002), mainly because they reported a value of ~–10° for the ecliptic latitude. Nevertheless, their rather preliminary pole solutions based on an ellipsoidal shape model assumption are relatively close to both our pole solutions and to the one of Ansdell et al. (2014) (Tab. 3).

The overall shape that corresponds to the first pole solution could evoke similarity to the spinning top shapes of some near-Earth primaries (e.g., asteroid (66391) 1999 KW_4, Ostro et al. 2006), however, the equatorial ridge in our case is not that obvious and symmetric. On the other hand, the second shape model is more angular and seems to us rather less realistic.

4.2. Thermophysical properties and size

As described in Section 2.2, we obtained three different datasets of thermal infrared measurements, namely from the IRAS satellite, the work of Green et al. (1985), and the Spitzer space telescope.

The absolute magnitude H and slope parameter G are necessary input parameters for the thermophysical modeling. G is used to compute geometric visible albedo p_V from the bolometric Bond albedo A ($A \approx (0.290+0.684G)\, p_V$, Bowell et al. 1989), which is one of the fitted parameters in the TPM, and H is a connection between p_V and size D. There are several, often inconsistent, values of H and G reported in the literature, thus our choice of reliable values needs careful justification. Values of H from MPC (14.6), AstDyS (14.17) and JPL (14.51) are provided with an assumed value of G (0.15). However, these absolute magnitudes are based on astrometric data from sky surveys that have poor photometric accuracy. Additionally, Pravec et al. (2012) found that absolute magnitudes (for asteroids with $H > 14$) derived from astrometric surveys have an average systematic offset of about −0.4 magnitude.

Our lightcurves obtained during three nights in Ondřejov in 2004 (see Tab. 1) were calibrated in the Cousins R system and span phase angles of 12.2–28.0 deg. Based on these data, values of H_R=13.93±0.04 and G=0.15±0.03 were derived. To transform the magnitude to the V filter, we derived the Johnson-Cousins V–R color index from the visible spectra of Licandro et al. (2007) as 0.331. Moreover, the V–R color index of Phaethon was also derived by Skiff et al. (1996), Dundon (2005) and Kasuga & Jewitt (2008): 0.34, 0.35±0.01 and 0.34±0.03, respectively. Applying a mean of all four values (0.34±0.01) resulted as H=14.27±0.04.

Another reliable absolute magnitude determination is reported by Wisniewski et al. (1997), where the authors observed Phaethon in the Johnson V filter at a phase angle of 21.6 deg. They provided H=14.51±0.14 with an assumed G=0.23±0.12.

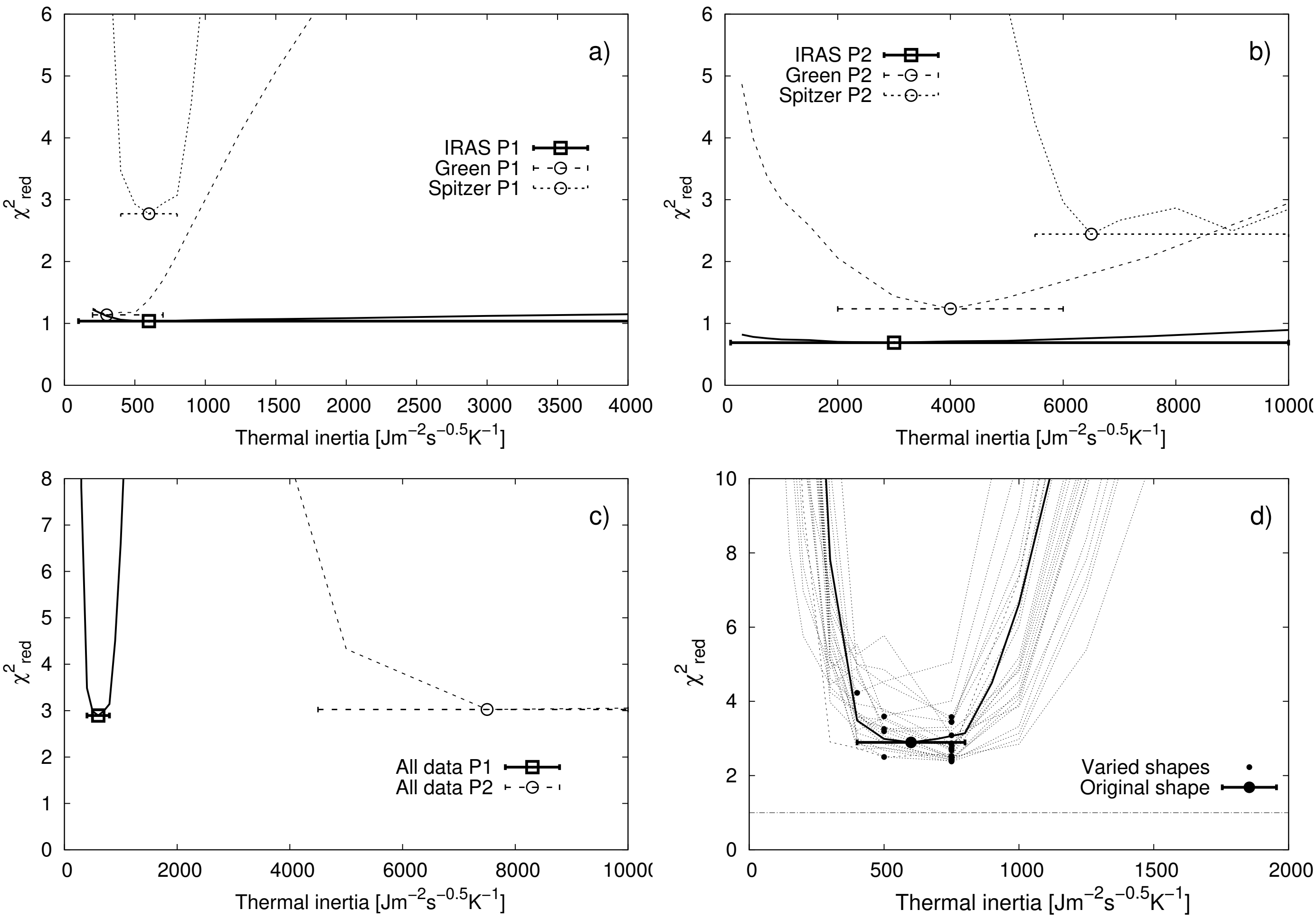

Fig. 6. Thermophysical fit in the thermal inertia parameter subspace: a) for all three thermal IR datasets (i.e., IRAS, Green, and Spitzer) individually with the first shape model as an input, b) for all three thermal datasets individually with the second shape model as an input, c) for the combined thermal dataset with both shape models as inputs, and finally d) for the combined thermal IR dataset and the original and the nominal shape model with 29 close variants (we show only the results based on the first, strongly preferred, shape model).

We corrected their H value to our G parameter and obtained H=14.41±0.06.

Finally, we computed a weighted mean from these two estimates and used H=14.31 and G=0.15 in the TPM modeling.

To be complete, Ansdell et al. (2014) reported absolute magnitude and slope from their optical data obtained in Cousins R filter. However, they claim that they were not able to calibrate several epochs because Phaethon was not in a Sloan field, but those data seem to be included in the phase curve fit. We decided not to use these estimates of H and G since the calibration of the data could not be verified. Nevertheless, their value of H_R=13.90 is consistent with our determination of H_R=13.93±0.04.

As a first step, we decided to apply the TPM to all three thermal datasets individually. This should allow us to validate the quality of each dataset, and potentially detect any inconsistency in the data.

IRAS fluxes have large uncertainties of ∼10–20%. Such values in absolute terms are even larger than the expected variability of the thermal lightcurve because of the rotation. As a result, the thermophysical modeling did not reasonably constrain any of the searched parameters. The fit in the thermal inertia subspace is shown in panels a) and b) of Fig. 6. For both shape models, we obtained a TPM fit with reduced chi-square of ∼1, where values of thermal inertia from ∼100 to several thousands J m^{-2}s$^{-1/2}$K^{-1}are statistically indistinguishable. The size and albedo are constrained only poorly.

The flux uncertainties in the Green et al. (1985) dataset are usually ∼5–10%, which proved to be sufficient to weakly constrain the thermophysical properties of Phaethon. The fit in thermal inertia for both shape models is shown in panels a) and b) of Fig. 6. Surprisingly, each shape model provides a different thermal inertia: the TPM fit with the first pole solution is consistent with values of Γ ∼200–700 J m^{-2}s$^{-1/2}$K^{-1}, but the fit with the second one suggests Γ >2 000 J m^{-2}s$^{-1/2}$K^{-1}. Such high values are suspicious, because they are significantly higher than measured for any other asteroid (Delbo' et al. 2015). On top of that, Opeil et al. (2010) provide upper limits for Γ of CM and CK4 chondritic meteorite materials, both proposed as likely analogs of Phaethon. Thermal inertia values for either CM (<650 J m^{-2}s$^{-1/2}$K^{-1}) and CK4 (<1 400 J m^{-2}s$^{-1/2}$K^{-1}) are much smaller than our lower limit of ∼2 000 J m^{-2}s$^{-1/2}$K^{-1}derived for the second pole solution. Because the first shape model was already slightly preferred based on the lightcurve dataset, the unusually high thermal inertia of the second model further supports this preference. Note that the derived geometric visible albedo of ~0.14 (second pole solution) is higher than all previously reported values (~0.11), and that the best-fitting parameters correspond to a fit with a reduced chi-square of ∼1.

The quality of thermal data from Spitzer compared to those from IRAS and Green et al. (1985) is superior. Thus, as expected, the TPM fit constrained thermal inertia, size, albedo and surface roughness quite well. However, the minimum reduced chi-square is ∼3, but this can be attributed to weak absorption and emission features in the spectra that are not included in our TPM model as our TPM models the thermal IR continuum. The interpretation of the emission spectra is an object of our forthcoming publication. Note that the thermal inertia derived from the Spitzer data is generally similar to the one from the Green et al. data, but the physical properties are better constrained. The thermal inertia is ~400–800 J $m^{-2}s^{-1/2}K^{-1}$ for the first pole solution and >3 000 J $m^{-2}s^{-1/2}K^{-1}$ for the second one. Geometric visible albedo (~0.12) and size (~5.1 km) are consistent with previous estimates from the IRAS, AKARI and WISE measurements. Medium values for the macroscopic surface roughness are preferred by the TPM (same as for the Green et al. data). Again, the first pole solution is preferred, because it has more realistic thermal inertia. Note that geometric visible albedo of the second pole solution is again rather high (~0.14).

All derived thermophysical parameters are summarized in Tab. 4. The parameter uncertainties reflect the range of all solutions that have reduced χ^2 values within the 1-sigma interval. Moreover, we also accounted for the uncertainty in the H value (estimated as ±0.05 mag) that contributes to the albedo uncertainty by ±0.006. On top of that, systematic errors in the model (i.e., lightcurve inversion, TPM) and data also likely affect parameter uncertainties. However, their contribution is difficult to estimate and thus is not accounted for in our final values.

Due to the superior quality of the Spitzer data, the TPM fit of combined Spitzer, IRAS and Green et al. thermal data is similar to the fit with Spitzer data only (see the fit in thermal inertia in panel c) of Fig. 6 and parameter values in Tab. 4).

Motivated by the findings of Hanuš et al. (2015) that the TPM results could be affected by the uncertainty in the shape model, we performed the varied-shape TPM modeling to check the stability of our TPM results based on fixed shape models as inputs. We bootstrapped the photometric dataset and constructed 29 shape models (by lightcurve inversion) that map the uncertainty in the shape and rotation state. As we have shown that the second pole solution/shape model can be rejected (because it results in unreasonably high thermal inertia), we performed the TPM only with the 29 shapes that correspond to the first shape solution. The fits in thermal inertia for the 29 bootstrapped/varied shape models, as well as for the original one, are shown in panel d) of Fig. 6. The best-fit thermal inertias all cluster around the original value ~600, indicating that this result is robust against shape uncertainties. Nevertheless, including shape uncertainties does propagate through to slightly larger uncertainties in the fitted parameters.

To summarize, we derived a size of D=5.1±0.2 km that is consistent with previous estimates. Moreover, our geometric visible albedo of p_V=0.12±0.01 is close to those reported (~0.11) as well. Our value of thermal inertia of Γ=600±200 J m^{-2} $s^{-1/2}$ K^{-1} is in agreement with those typical for small near-Earth asteroids with size ranging from a few hundred meters to few kilometers, maybe slightly on the high end (Delbo' et al. 2015). The intuitive interpretation of the relatively high thermal inertia value is that small bodies had short collisional lifetime and thus developed only a coarse regolith (Delbo' et al. 2007). On the other hand, larger objects with much longer collisional lifetime had enough time to build a layer of fine regolith which results in smaller values of thermal inertias. In the case of Phaethon, the close perihelion distance might lead to solar wind fluxes high enough to directly remove any fine regolith from the surface. This could also explain the observed brightening near perihelion due to dust particles with an effective diameter of ∼1 μm (Jewitt et al. 2013).

4.3. Orbital and spin axis evolution of Phaethon

Orbital and rotational motion of celestial bodies are generally not independent. Many examples of their mutual coupling have been discussed in planetary astronomy (e.g., the spin vector alignments of asteroids in the Koronis family, or the spin state study in the Flora family, Vokrouhlický et al. 2003; Vraštil & Vokrouhlický 2015). Here we deal with one particular aspect of these effects, namely how orbital motion influences long-term evolution of rotational motion. Our aim is to make use of our pole solutions from Sec. 4.1 and investigate conditions of Phaethon's surface harsh irradiation near the pericenter of its orbit during the past tens of kyrs.

4.3.1. Orbital evolution

To start our analysis we first need to obtain information about Phaethon's orbit evolution. For sake of our argument we are only interested in a certain time interval before the current epoch (somewhat arbitrarily we chose 1 Myr). We are aware of a strong chaoticity of the orbit evolution due to planetary encounters. Therefore, our results are just examples of possible past orbital histories of Phaethon. It is, however, important to note that the secular spin evolution is mostly sensitive to the orbital inclination and nodal longitude evolution, which are less affected by the random component in planetary effects.

We used a well-tested software package `swift`[2] to numerically integrate the nominal orbit of Phaethon, its clone variants, and the planets. All bodies were given their initial conditions at epoch MJD 57 400: planets from the JPL DE405 ephemerides and the asteroid from the orbit solution provided by the `AstDyS` website maintained at the University of Pisa. The asteroid close clones were created using the full covariant matrix of the `AstDyS` solution. Because of Phaethon's rich observational record, the close clones differ from the nominal orbit by only very tiny values in all orbital elements (for instance, $\sim 2\times10^{-9}$ in semimajor axis, $\sim 2\times10^{-8}$ in eccentricity or $\sim 3\times10^{-7}$ in inclination, all fractional values). As a result, the nominal solution does not have a special significance, and Phaethon might have followed any of the clone orbits. The backward integration in time was dealt with by inverting the sign of velocity vectors. We used a short timestep of 3 days and output state vectors of all bodies every 50 years. This is a sufficient sampling for spin vector integrations described in Sec. 4.3.2. We integrated all bodies to 1 Myr. We included gravitational perturbations from planets, but neglected all effects of non-gravitational origin (such as recoil due to ejection of dust or gas particles and the Yarkovsky effect). For our purposes, however, this approximation is sufficient.

The evolution of Phaethon's orbit is shown in Fig. 7. Looking first at a longer timescale presented in the left column of plots, we note that the orbital semimajor axis evolution is dominated by random-walk effects induced by the brief gravitational tugs due to planetary encounters. The evolution of eccentricity and

[2] `http://www.boulder.swri.edu/~hal/swift.html`.

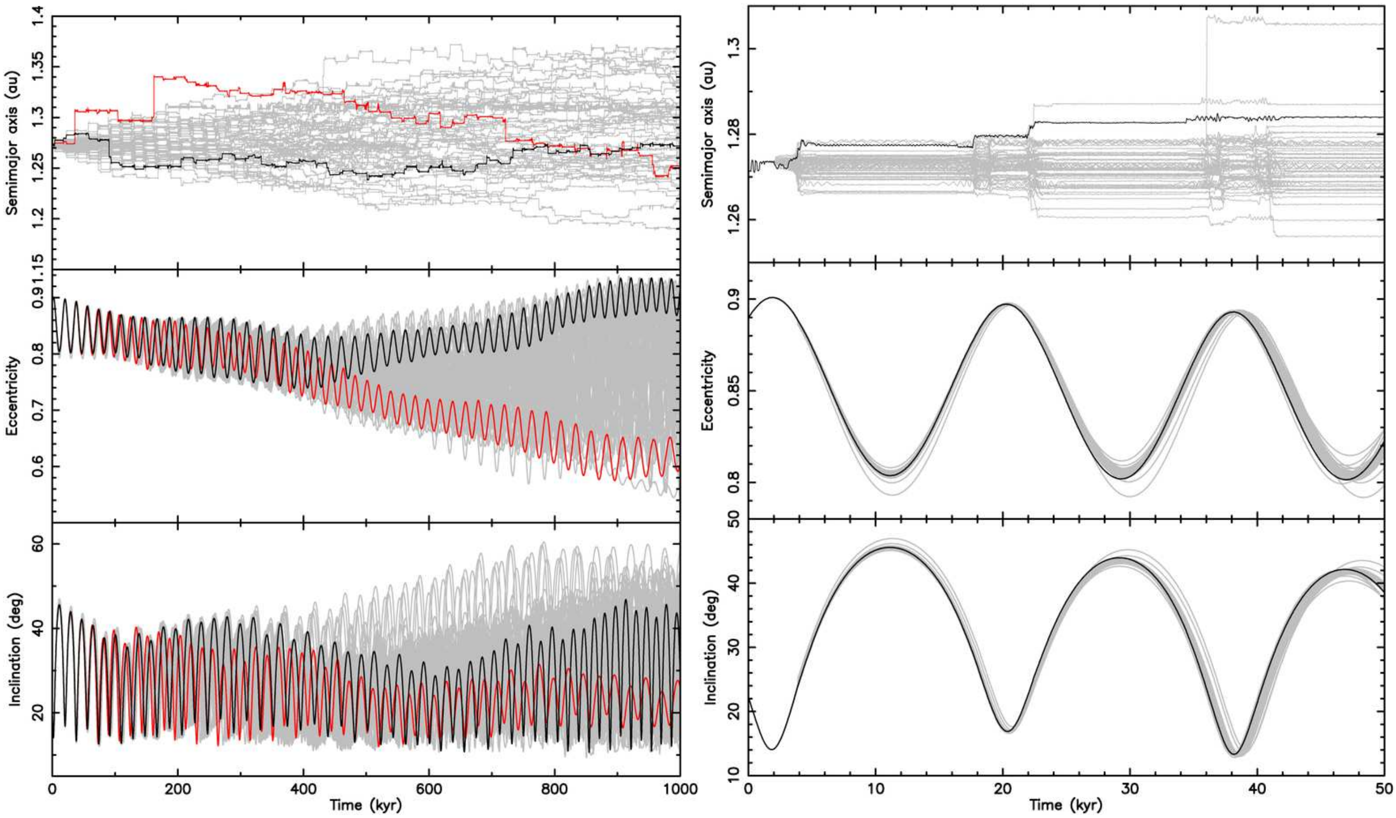

Fig. 7. Past dynamical evolution of Phaethon's orbit: (i) semimajor axis (top), (ii) eccentricity (middle), and (iii) inclination (bottom). Left panels show the whole integrated timespan of 1 Myr, right panels show just the first 50 kyr – in both cases time goes to the past. We show the nominal orbit (black line), and also orbits of the 50 clones (gray lines). Note that the true past orbital evolution might have been any of those histories. Moreover, red lines represent clone evolution with eccentricity steadily decreased to the past.

inclination is different in nature from the semi-major axis evolution. While also indicating a significant divergence of clone orbits, especially past ~ 100 kyr time mark, the planetary encounters do not produce noticeable perturbations directly in eccentricity or inclination. Rather, their effect on e and i is indirect, being due to changes of secular frequencies reflecting the semimajor axis accumulated perturbation. Given the semimajor axis chaoticity, the eccentricities and inclination may also undertake diverse evolutions on a long term. For instance, the eccentricity might have stayed very high (as in the case of the nominal solution, black line), or steadily decreased to the past (selected clone shown by the red line). Overall though, we note that the eccentricity of Phaethon's orbit has been increasing on average for all clone solutions during the past ~ 300 kyr.

The right column of plots in Fig. 7 shows how the orbital solution for Phaethon and its clones behaves on a much shorter timescale, namely the past 50 kyr only. The semimajor axis evolution still shows a clear traits of planetary encounters with a significant onset of divergence some 4 kyr ago. Eccentricities and inclinations, however, are much more stable. We may appreciate the indirect planetary effect discussed above. For instance the principal secular frequency of the inclination and node is among the fastest for the nominal solution and slower for many of the clone solutions (see how the inclination solution for clones trails in time behind the nominal inclination oscillations). This is because the nominal solution happens to have the largest semimajor axis, while most of the clones were scattered to smaller semimajor axis values. About 2 kyr ago Phaethon's orbital eccentricity was at its maximum, making its perihelion value reach $q \sim 0.126$ au, significantly smaller than its current value $q \sim 0.14$ au. Actually, this has been already noted before (e.g., Williams & Wu 1993). Several authors studied a possibility of a recent formation of the Geminids stream, including that near 0 AD when the perihelion had its last minimum (see, e.g., Ryabova 2007 or, for a more detailed overview, Jenniskens 2006). However, a detailed match of the observed activity of Geminids over years may require particle feeding over an extended interval of time (Jewitt et al. 2015). Note also, that the perihelion distance might not be the only parameter relevant to Phaethon's activity. It is possible that the spin axis orientation, studied in Sec. 4.3.2, plays an equally important role. Note that the maximum eccentricity values during the previous cycles (i.e., about 20 kyr ago and 38 kyr ago) were smaller and the perihelion was comparable to its current value. As mentioned above, this trend of decreasing eccentricity continues to about 300 kyr ago.

It is also interesting to consider asteroids (155140) 2005 UD and (225416) 1999 YC. These two objects have been discussed as Phaethon's twins in the literature (e.g., Ohtsuka et al. 2006, 2008, 2009), perhaps fragments chopped off a common parent body of Phaethon and the Geminid complex. Considering a tighter-related orbit of 2005 UD, we repeated our backward integration of a nominal orbit and 50 close clones. We confirm proximity of the orbital evolution with that of Phaethon. However, the difference in orbital secular angles (longitudes of node and perihelion) prevents separation of (155140) from Phaethon in the immediate past (see also Ohtsuka et al. 2006). We estimate these two objects might have separated from a common parent body

$\sim$ 100 kyr ago or, more likely, even before this epoch. So these kilometer-sized bodies, possibly related to Phaethon, must have a genesis in a different event in history than the current Geminid stream.

Additionally, Kinoshita et al. (2007) reports that 2005 UD has $(B-V)$, $(V-R)$ and $(R-I)$ color indices similar to those of Phaethon. As they are very rare colors (bluish spectral slope), it appears unlikely that the two asteroids could be just a random coincidence; rather, it supports the suggestion that they are genetically related. It is also interesting that the asteroid pair Phaethon–2005 UD has the primary spin period (3.6 h) and the size ratio (estimated from their absolute magnitude difference of 3.0) in agreement with the model of spin-up fission formation of asteroid pairs Pravec et al. (2010). This suggests that 2005 UD was formed from material escaped from Phaethon after it was spun up to the critical rotation rate (presumably by YORP).

4.3.2. Spin evolution

We use the secular model of the asteroid rotation-state evolution formulated in Breiter et al. (2005). In this framework, all dynamical effects with periods shorter than rotational and orbital periods are eliminated by averaging, and the spin evolution is considered on long-timescales. This is not only sufficient for our work here, but it also considerably speeds up numerical simulations. We include the gravitational torque due to the Sun and, again, neglect all effects of non-gravitational origin. This implies that the mean rotation period is conserved and the evolution is principally described by changes in direction **s** of the spin axis. The importance of the model arises due to the fact that the heliocentric orbit evolves by the planetary perturbations as has been described in the previous Section. The characteristic timescale of the spin axis precession in space due to the solar torque may be similar to that of the orbit precession about the pole of ecliptic. If so, interesting resonant phenomena may occur and produce a complicated evolution of asteroid's rotational pole (e.g., Vokrouhlický et al. 2006).

Our torque model is only approximate and should be made more accurate in the future if observations would require it. In particular, the Yarkovsky-O'Keefe-Radzievskii-Paddack (YORP) effect could be estimated when (i) the shape model and spin state is improved, and (ii) photometry over a longer timespan is available. At present, our conclusions and test runs do not require YORP effect included in the model. For instance, using our preferred pole and shape model for Phaethon we estimate that in 1 Myr the rotation period would change by few percents and obliquity by less than ten degrees only. We used a simple, one-dimensional model presented in Čapek & Vokrouhlický (2004) and bulk density of 1 g cm^{-3}. The main factor that diminishes importance of the YORP effect is Phaethon's large size.

Conveniently, Breiter et al. (2005) also provide an efficient symplectic integration scheme for spin axis evolution. Apart from the initial direction of **s** at some chosen epoch, the model needs two ingredients. First, the orbit evolution due to planetary perturbations is required. In our case, this is provided by the numerical integrations above. Second, we need to know the precession constant of the asteroid. For a given rotation period its value depends on a single parameter, usually called dynamical ellipticity $\Delta = (C - 0.5(A + B))/C$, where A, B, and C are principal moments of the inertia tensor of the body. In principle, Δ can be estimated from our shape models obtained by the lightcurve inversion in Sec. 4.1. Our nominal models for both pole solution yield $\Delta \simeq 0.11$. However, shape variants that are still compatible with the fit to available lightcurves could provide Δ values in the 0.06 to 0.16 interval. We use this range as the uncertainty of Phaethon's Δ value.

Propagation of Phaethon's spin vector **s** is subject to uncertainty that originates from several sources. First, the initial conditions are not exact. We assume 5° uncertainty in both ecliptic longitude and latitude of our two nominal pole solutions from Sec. 4.1. Because we found that one of the nominal pole solutions provides a more satisfactory thermal inertia value (thereafter denoted P1), we study spin histories starting in its vicinity first. Then we proceed with those starting in the vicinity of the second nominal pole solution (thereafter denoted P2). Second, the dynamical ellipticity has $\simeq \pm 0.05$ uncertainty. Third, the orbit may follow any of the clone variants described in Sec. 4.3.1. Our tests show that the third issue is the least important (at least on a timescale we are interested in). For simplicity, we thus assume our nominal solution of Phaethon's orbital evolution only, and consider *spin clones* by propagating **s** from (i) different initial conditions, and (ii) with different Δ values. As in the case of orbital clones above, the past spin evolution of Phaethon may follow any of the clone solutions with equal statistical likelihood. We integrate spin evolution to 1 Myr backward in time, the same interval for which we have integrated the orbit. The timestep is 50 yr, sufficient to describe secular effects.

To communicate the results of the integrations in a simple way, we use two angular variables related to the **s** direction. First, we use the obliquity ε, namely the angle between **s** and the normal to the osculating orbital plane. The obliquity directly informs us about the sense of Phaethon's rotation, and it is important for some orbital accelerations of non-gravitational origin (such as the Yarkovsky effect). Second, we also determine the angle α between **s** and direction to the Sun *at perihelion* of the orbital motion. The angle α is important parameter determining which hemisphere of Phaethon is preferentially irradiated near perihelion (e.g., $\alpha \ll 90°$ implies northern hemisphere receives most of the solar radiation at pericenter an vice versa).

Figure 8 shows our results. We focus first on our preferred pole solution P1 with initial ecliptic longitude $\lambda \simeq 319°$ (left column). The obliquity exhibits stable oscillations about the mean value $\sim$ 148° with typically a small amplitude of $\sim$ 10°, much less than the orbit inclination. This is because the spin axis precession frequency due to the solar gravitational torque is much faster than the orbit-plane precession frequency. Additionally, the sense of precession is opposite for retrograde rotation ($\varepsilon >$ 90°). Obliquity of just one exceptional spin clone shows irregular excursions to $\sim$ 40°, being thus temporarily prograde before returning back to the retrograde-rotation zone. This phenomenon is due to the existence of a large chaotic zone associated with Cassini secular resonance between the spin axis precession and orbital precession with the mean frequency $\simeq -32.5$ arcsec/yr. While the nominal resonant obliquity is $\simeq$ 84.5°, the resonant zone extends from $\simeq$ 30° to $\simeq$ 120° obliquity (see Vokrouhlický et al. 2006, for more examples). Therefore, the nominal pole solution P1 is barely safe from these chaotic effects. The angle α between **s** and direction to the Sun at perihelion also shows rather stable oscillations about a mean value of $\simeq$ 90°. Looking at the past 50 kyr of evolution (bottom left plots at Fig. 8), we see that the current value of $\simeq$ 98.8° switches to about 60° some $\simeq$ 2 kyr ago. Therefore, when the perihelion was the lowest ($\sim$ 0.126 au), the northern hemisphere of Phaethon was harshly irradiated by sunlight at perihelion. But the values of α oscillate up and down from $\simeq$ 50° to about $\simeq$ 130°. Thus $\simeq$ 500 yr ago, and again $\simeq$ 4 kyr ago, it was the southern hemisphere's turn to be irradiated at perihelion. We believe this is the reason why Phaethon's surface does not show any convincing hemispheric spectral or color asymmetry (Ohtsuka et al. 2009). Additionally, we wonder whether these polar-irradiation cycles, together with variations in perihelion distance, play a role in the strength of Phaethon's activity and thus possibly in the origin of different components of the Geminids stream.

In the case of our second nominal pole solution with the initial ecliptic longitude $\lambda \simeq 84°$ (right column in Fig. 8) things go more wild. This is because the initial obliquity $\simeq 126°$ is dangerously close to the chaotic layer of the above mentioned Cassini resonance. Indeed, even the nominal spin solution shown by the black line is dragged to the prograde-rotation zone of obliquities $< 90°$ at $\sim$ 300 kyr ago. Many spin clones follow similar evolution, though others stay safely in the retrograde-rotating region. As expected, the angle α between **s** and the solar direction at pericenter also exhibits much larger oscillations than in the P1 solution. In the P2 case the geometry is switched, such that currently the southern hemisphere is preferentially irradiated at the perihelion (e.g., Ohtsuka et al. 2009; Ansdell et al. 2014). However, $\simeq$ 2 kyr ago the geometry changes for the P2 solutions and the northern hemisphere was irradiated at the perihelion.

Finally, we would like to remove a slight misconception from Ansdell et al. (2014). The current $\varepsilon > 90°$ obliquity of Phaethon, holding for either of the P1 and P2 solutions, cannot be directly linked to the Yarkovsky transport from the main belt. At the moment Phaethon's precursor asteroid was leaving the main belt zone, as envisaged for instance by de León et al. (2010), the rotation state was likely retrograde (only retrograde members of the Pallas collisional family can enter the 8:3 mean motion resonance, which corresponds to the most probable dynamical pathway of Phaethon). However, in millions of years when the orbit was evolving in the planet-crossing zone, the obliquity might have undergone chaotic evolution driven by Cassini spin-orbit resonances and the YORP effect. Note, for instance, that the nominal P2 solution in Fig. 8 indeed goes through a transition from prograde to retrograde regime in the last 1 Myr of evolution.

5. Conclusions

28 lightcurves are presented in this paper using six different telescopes (65cm in Ondřejov, UH88 in Hawaii, 60cm in Modra, 1m in Calern, IAC-80 at Teide, and 66cm at Badlands Observatory) between November 2, 1994 and October 8, 2015.

We derive a unique shape model of NEA (3200) Phaethon based on previous and newly obtained lightcurves. This model will be useful for planning the observations during the December 2017 close approach (as close as 0.069 au to the Earth). Although two pole solutions are consistent with the optical data, only the formally better solution – sidereal rotation period of 3.603958(2) h and ecliptic coordinates of the preferred pole orientation of $(319\pm5, -39\pm5)°$ – provides a TPM fit of the thermal (mid-)infrared data with realistic thermophysical parameters.

Our newly obtained lightcurves, their comparison with the modeled lightcurves, and the shape model are available in the Database of Asteroid Models from Inversion Techniques.

By applying a thermophysical model to thermal fluxes from the IRAS satellite and Green et al. (1985), and mid-infrared spectra from the Spitzer space telescope, we derive size (D=5.1±0.2 km), geometric visible albedo (p_V=0.122±0.008), thermal inertia (Γ=600±200 J m^{-2}s$^{-1/2}$K^{-1}) and medium surface roughness for Phaethon. These values are consistent with previous estimates. The derived thermal inertia is slightly higher than for those of similarly sized near-Earth asteroids, however, still consistent.

Based on our study of a long-term orbital evolution of Phaethon, we confirm previous findings that about 2 kyr ago Phaethon's orbital eccentricity was at its maximum, making its perihelion value reach $q \sim 0.126$ au, significantly smaller than its current value $q \sim 0.14$ au. The eccentricity of Phaethon's orbit has been increasing on average for all clone solutions during the past $\sim$ 300 kyr. Both behavior could be relevant for the origin of Geminids. Note that the maximum eccentricity values during the previous (oscillating) cycles (i.e., about 20 kyr ago and 38 kyr ago) were smaller and the perihelion was comparable to its current value.

We confirm proximity of the orbital evolution of asteroids (155140) 2005 UD and (225416) 1999 YC with that of Phaethon. However, the difference in orbital secular angles (longitudes of node and perihelion) prevents their separation from Phaethon in the immediate past (see also Ohtsuka et al. 2006), but rather $\sim$ 100 kyr ago or, more likely, even before this epoch. So these kilometer-sized bodies are likely not related to the current Geminid stream. The similarities in color indices of Phaethon and 2005 UD and their size ratio further supports the existence of the Phaethon–2005 UD asteroid pair.

The obliquity of the preferred spin solution exhibits stable oscillations about the mean value $\sim 148°$ with typically a small amplitude of $\sim 10°$, much less than the orbit inclination. The existence of a large chaotic zone associated with Cassini secular resonance between the spin axis precession and orbital precession can temporarily switch the rotation to a prograde one. While this behavior is rare for the preferred pole solution, it is very common for the second pole solution.

When the perihelion was the lowest about 2 kyr ago ($\sim$ 0.126 au), the northern hemisphere of Phaethon (preferred pole solution) was harshly irradiated by sunlight at perihelion. On the other hand, $\simeq$ 500 yr ago, and again $\simeq$ 4 kyr ago, it was the southern hemisphere's turn to be irradiated at perihelion. This likely explains the lack of any convincing hemispheric spectral or color variations (Ohtsuka et al. 2009).

Acknowledgements. JH greatly appreciates the CNES post-doctoral fellowship program. The work of DV and PP was supported by the Czech Science Foundation (grants GA13-01308S and P209-12-0229). The work of VAL is performed in the context of the NEOShield-2 project, which has received funding from the European Union's Horizon 2020 research and innovation programme under grant agreement No. 640351. MD and VAL were also supported by the project under the contract 11-BS56-008 (SHOCKS) of the French Agence National de la Recherche (ANR). The work at Modra is supported by the Slovak Grant Agency for Science VEGA (Grant 1/0670/13).

This article is based on observations made with the IAC-80 operated on the island of Tenerife by the Instituto de Astrofísica de Canarias in the Spanish Observatorio del Teide. JL acknowledges support from the project ESP2013-47816-C4-2-P (MINECO, Spanish Ministry of Economy and Competitiveness).

The authors wish to acknowledge and honor the indigenous Hawaiian community because data used in this work were obtained from the summit of Maunakea. We honor and respect the reverence and significance the summit has always had in native Hawaiian culture. We are fortunate and grateful to have had the opportunity to conduct observations from this most sacred mountain.

This work is based in part on observations made with the Spitzer Space Telescope, which is operated by the Jet Propulsion Laboratory, California Institute of Technology under a contract with NASA. Support for this work was provided by NASA through an award issued by JPL/Caltech.

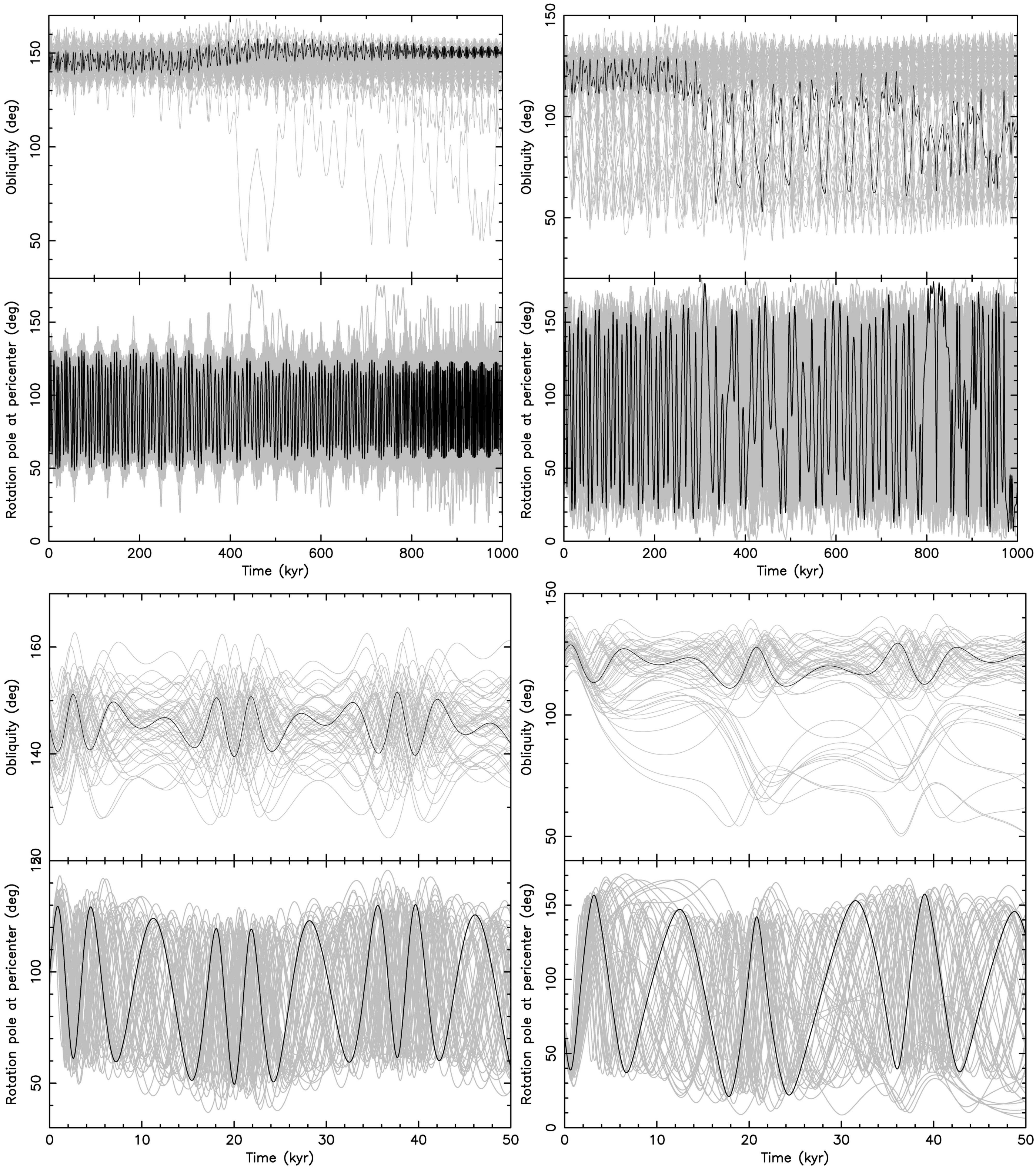

Fig. 8. Past dynamical evolution of Phaethon's spin axis direction **s**: left column of panels for the P1 solution $(\lambda, \beta) = (319°, -39°)$, right column of panels for the P2 solution $(\lambda, \beta) = (84°, -39°)$. The upper two panels show spin evolution over the whole integrated interval of 1 Myr, the bottom two panels zoom at the past 50 kyr. Each time the nominal solution is shown by the black line, while the gray lines are for the 50 spin clones (see the text). Each of the four sections shows (i) the obliquity ε at the top (angle between **s** and normal to the osculating orbital plane), and (ii) the angle α between **s** and direction to the Sun at pericenter.

Table 1. List of dense-in-time lightcurves used for the shape modeling. For each lightcurve, the table gives the epoch, number of points N_p, asteroid's distances to the Sun r and Earth Δ, used filter and telescope, observer, and reference.

N	Epoch	N_p	r [au]	Δ [au]	Filter	Telescope	Observer	Reference
1	1989-10-09.4	30	2.02	1.22	V	90 inch Steward Observatory	Wisniewski	Wisniewski et al. (1997), rejected
2	1994-11-02.1	22	1.82	1.04	R	D65	Pravec	This work
3	1994-12-02.9	14	1.53	0.56	R	D65	Pravec	This work
4	1994-12-04.1	17	1.51	0.54	R	D65	Pravec	This work
5	1994-12-06.9	13	1.48	0.52	R	D65	Pravec	This work
6	1994-12-27.3	76	1.22	0.44	R	Lowell	Buie	Ansdell et al. (2014)
7	1995-01-04.4	11	1.10	0.46	R	UH88	Meech, Hainaut	Ansdell et al. (2014)
8	1995-01-04.8	45	1.10	0.46	R	Ondřejov	Pravec	Pravec et al. (1998)
9	1995-01-05.4	79	1.09	0.46	R	UH88	Meech, Hainaut	Ansdell et al. (2014)
10	1997-11-01.1	88	1.32	0.78	R	Ondřejov	Pravec	Pravec et al. (1998)
11	1997-11-02.1	80	1.31	0.76	R	Ondřejov	Pravec	Pravec et al. (1998)
12	1997-11-11.6	39	1.18	0.56	R	UH88	Meech, Bauer	Ansdell et al. (2014)
13	1997-11-12.6	52	1.16	0.54	R	UH88	Meech, Bauer	Ansdell et al. (2014)
14	1997-11-21.6	48	1.02	0.39	R	UH88	Meech, Bauer	Ansdell et al. (2014)
15	1997-11-22.6	47	1.01	0.37	R	UH88	Meech, Bauer	Ansdell et al. (2014)
16	1997-11-25.6	24	0.95	0.34	R	UH88	Meech, Bauer	Ansdell et al. (2014)
17	1998-11-22.1	14	2.31	1.36	R	IAC-80	Licandro	This work
18	1998-11-23.1	16	2.31	1.36	R	IAC-80	Licandro	This work
19	1998-12-08.0	9	2.26	1.39	R	IAC-80	Licandro	This work
20	1998-12-09.0	15	2.25	1.40	R	IAC-80	Licandro	This work
21	2003-11-20.8	18	1.76	0.81	R	Ondřejov	Pravec, Kušnirák	This work, rejected
22	2004-11-13.3	12	1.84	0.89	R	Badlands Observatory	Reddy, Dyvig	This work, rejected
23	2004-11-19.5	38	1.78	0.83	R	UH88	Dundon	Ansdell et al. (2014)
24	2004-11-21.6	51	1.76	0.81	R	UH88	Dundon	Ansdell et al. (2014)
25	2004-11-22.4	35	1.75	0.80	R	UH88	Dundon	Ansdell et al. (2014)
26	2004-11-25.1	47	1.73	0.76		Modra	Galád	This work, rejected
27	2004-12-05.0	101	1.63	0.67	R	D65	Pravec, Kušnirák	This work
28	2004-12-05.3	41	1.63	0.67	R	Badlands Observatory	Reddy, Dyvig	This work
29	2004-12-11.0	148	1.57	0.64	R	D65	Pravec, Kušnirák	This work
30	2004-12-18.8	15	1.48	0.61	R	D65	Pravec, Kušnirák	This work
31	2007-11-17.2	47	1.28	0.51		Modra	Galád	This work
32	2007-11-28.2	96	1.13	0.29		Modra	Galád	This work
33	2007-12-04.1	232	1.03	0.18		Modra	Kornoš, Világi	This work
34	2013-11-20.3	24	1.07	0.80	R	UH88	Dundon	Ansdell et al. (2014)
35	2013-11-23.3	16	1.12	0.84	R	UH88	Ansdell	Ansdell et al. (2014)
36	2013-12-03.2	20	1.26	1.02	R	Lowell	Meech, Ansdell	Ansdell et al. (2014)
37	2013-12-11.3	36	1.37	1.18	R	UH88	Ansdell	Ansdell et al. (2014)
38	2014-11-27.3	89	1.82	0.85		CS3-PDS	Warner	Warner (2015)
39	2014-11-28.2	84	1.81	0.85		CS3-PDS	Warner	Warner (2015)
40	2014-11-28.4	58	1.81	0.84		CS3-PDS	Warner	Warner (2015)
41	2014-11-29.3	82	1.80	0.84		CS3-PDS	Warner	Warner (2015)
42	2014-11-29.5	27	1.80	0.84		CS3-PDS	Warner	Warner (2015)
43	2014-12-10.1	91	1.71	0.78	R	C2PU	Devogèle	This work
44	2014-12-11.9	92	1.69	0.77	R	C2PU	Devogèle	This work
45	2014-12-14.2	52	1.67	0.77		CS3-PDS	Warner	Warner (2015)
46	2014-12-15.3	73	1.66	0.77		CS3-PDS	Warner	Warner (2015)
47	2015-01-13.9	54	1.32	0.83	R	C2PU	Rivet, Hanuš, Delbo'	This work
48	2015-01-17.9	50	1.27	0.85	V	C2PU	Devogèle	This work
49	2015-02-09.8	30	0.91	0.89	V	C2PU	Devogèle	This work
50	2015-02-10.8	41	0.89	0.89	V	C2PU	Devogèle	This work
51	2015-02-11.8	39	0.87	0.89	V	C2PU	Devogèle	This work
52	2015-08-21.6	26	2.15	2.09	R	UH88	Bolin	This work
53	2015-09-08.6	22	2.24	1.90	R	UH88	Bolin	This work
54	2015-09-09.6	30	2.24	1.89	R	UH88	Bolin	This work
55	2015-10-08.5	21	2.33	1.60	R	UH88	Bolin	This work

Table 2. Thermal infrared measurements available for Phaethon. For each measurement, the table gives the light-time corrected epoch in Julian date, wavelength λ, filter, flux with its error, asteroid's distances to the Sun r and Earth Δ, and reference to the source.

Epoch (LT corr) JD	λ [μm]	Filter	Flux [Jy]	Flux err [Jy]	Δ au	r au	Reference
2 445 618.566846	12.0	I1	2.826	0.317	1.028	0.370	IRAS
2 445 618.566846	25.0	I2	3.453	0.563	1.028	0.370	IRAS
2 445 618.566846	60.0	I3	1.101	0.250	1.028	0.370	IRAS
2 445 618.781563	12.0	I1	2.377	0.272	1.032	0.371	IRAS
2 445 618.781563	25.0	I2	3.617	0.610	1.032	0.371	IRAS
2 445 618.781563	60.0	I3	1.161	0.241	1.032	0.371	IRAS
2 445 618.781563	100.0	I4	0.445	0.096	1.032	0.371	IRAS
2 445 618.853136	12.0	I1	2.143	0.245	1.033	0.371	IRAS
2 445 618.853136	25.0	I2	3.601	0.594	1.033	0.371	IRAS
2 445 618.853136	60.0	I3	1.232	0.279	1.033	0.371	IRAS
2 445 618.924708	12.0	I1	2.164	0.257	1.034	0.371	IRAS
2 445 618.924708	25.0	I2	3.024	0.493	1.034	0.371	IRAS
2 445 618.924708	60.0	I3	1.212	0.249	1.034	0.371	IRAS
2 445 618.996292	12.0	I1	1.964	0.242	1.035	0.371	IRAS
2 445 618.996292	25.0	I2	3.275	0.483	1.035	0.371	IRAS
2 445 618.996292	60.0	I3	1.087	0.219	1.035	0.371	IRAS
2 445 619.067876	12.0	I1	1.852	0.255	1.036	0.372	IRAS
2 445 619.067876	25.0	I2	3.116	0.455	1.036	0.372	IRAS
2 445 619.067876	60.0	I3	1.007	0.237	1.036	0.372	IRAS
2 446 054.797880	10.6	N	3.853	0.231	1.131	0.246	Green et al. (1985)
2 446 054.802080	19.2	Q	5.380	0.323	1.131	0.246	Green et al. (1985)
2 446 054.806880	4.7	M	0.174	0.030	1.131	0.246	Green et al. (1985)
2 446 054.810380	8.7	-	2.566	0.103	1.131	0.246	Green et al. (1985)
2 446 054.812480	9.7	-	3.175	0.190	1.131	0.246	Green et al. (1985)
2 446 054.815280	10.3	-	3.326	0.200	1.131	0.246	Green et al. (1985)
2 446 054.817380	11.6	-	4.296	0.215	1.131	0.246	Green et al. (1985)
2 446 054.820780	12.5	-	4.436	0.266	1.131	0.246	Green et al. (1985)
2 446 054.822880	10.6	N	3.450	0.207	1.131	0.246	Green et al. (1985)
2 446 054.854181	10.6	N	3.646	0.219	1.130	0.246	Green et al. (1985)
2 446 054.913881	4.7	M	0.194	0.016	1.129	0.246	Green et al. (1985)
2 446 055.831186	4.7	M	0.221	0.018	1.115	0.245	Green et al. (1985)

Table 3. Rotation state parameters derived for Phaethon by the lightcurve inversion from different photometric datasets. The table gives the ecliptic coordinates λ and β of all possible pole solutions, the sidereal rotational period P, and reference. The uncertainties in our pole solutions are 5 degrees.

λ_1 [deg]	β_1 [deg]	λ_2 [deg]	β_2 [deg]	P [hours]	Note
319	−39	84	−39	3.603958±0.000002	This work
		85±13	−20±10	3.6032±0.0008	Ansdell et al. (2014)
276	−15	97	−11	3.59060	Krugly et al. (2002)

Table 4. Thermophysical properties of asteroid Phaethon derived by the TPM from different thermal datasets based on two pole solutions. We also include the results based on the varied shape TPM approach (only first pole solution). The table provides volume equivalent diameter D, thermal inertia Γ, visual geometric albedo p_V, macroscopic surface roughness, the best fit χ^2_{red}, heliocentric distance r of Phaethon during its observation, and the thermal dataset used.

D [km]	Γ [J m^{-2}s$^{-1/2}$K^{-1}]	p_V	Roughness	χ^2_{red}	r [au]	Dataset
		Pole 1: λ=319°, β=−39°				
$6.0^{+0.5}_{-0.3}$	–	$0.09^{+0.04}_{-0.2}$	–	1.0	1.0	IRAS
$4.6^{+0.4}_{-0.2}$	300^{+400}_{-100}	$0.145^{+0.008}_{-0.013}$	Medium	1.1	1.1	Green et al. (1985)
$5.1^{+0.2}_{-0.2}$	600^{+200}_{-200}	$0.122^{+0.008}_{-0.008}$	Medium	2.8	1.1	Spitzer
$5.1^{+0.2}_{-0.2}$	600^{+200}_{-200}	$0.122^{+0.008}_{-0.008}$	Medium	2.9	~1.0	All
$5.1^{+0.3}_{-0.3}$	700^{+300}_{-300}	$0.12^{+0.01}_{-0.01}$	Medium	2.9	~1.0	VS-TPM All
		Pole 2: λ=84°, β=−39°				
$5.6^{+0.7}_{-0.5}$	–	$0.10^{+0.15}_{-0.02}$	–	0.7	1.0	IRAS
$5.3^{+0.5}_{-0.4}$	$4000^{+2\,000}_{-2\,000}$	$0.13^{+0.02}_{-0.02}$	High	1.2	1.1	Green et al. (1985)
$5.2^{+0.2}_{-0.2}$	$6500^{+3\,500}_{-1\,000}$	$0.14^{+0.01}_{-0.01}$	–	2.5	1.1	Spitzer
$4.9^{+0.2}_{-0.2}$	$7500^{+2\,500}_{-3\,000}$	$0.15^{+0.01}_{-0.01}$	–	3.0	~1.0	All

References

Alí-Lagoa, V., Lionni, L., Delbo', M., et al. 2014, A&A, 561, A45
Ansdell, M., Meech, K. J., Hainaut, O., et al. 2014, ApJ, 793, 50
Arendt, R. G. 2014, AJ, 148, 135
Bowell, E., Hapke, B., Domingue, D., et al. 1989, in Asteroids II, ed. R. P. Binzel, T. Gehrels, & M. S. Matthews, 524–556
Breiter, S., Nesvorný, D., & Vokrouhlický, D. 2005, AJ, 130, 1267
Campins, H., Kelley, M. S., Fernández, Y., Licandro, J., & Hargrove, K. 2009, Earth Moon and Planets, 105, 159
Čapek, D. & Vokrouhlický, D. 2004, Icarus, 172, 526
Chamberlin, A. B., McFadden, L.-A., Schulz, R., Schleicher, D. G., & Bus, S. J. 1996, Icarus, 119, 173
Chernetenko, Y. A. 2010, in Protecting the Earth against Collisions with Asteroids and Comet Nuclei, ed. A. M. Finkelstein, W. F. Huebner, & V. A. Short, 289
Chesley, S. R., Farnocchia, D., Nolan, M. C., et al. 2014, Icarus, 235, 5
Clark, B. E., Ziffer, J., Nesvorny, D., et al. 2010, Journal of Geophysical Research (Planets), 115, E06005
de León, J., Campins, H., Tsiganis, K., Morbidelli, A., & Licandro, J. 2010, A&A, 513, A26
Decin, L., Morris, P. W., Appleton, P. N., et al. 2004, ApJS, 154, 408
Delbo', M. 2004, PhD thesis - Freie Univesitaet Berlin, 1
Delbo', M., dell'Oro, A., Harris, A. W., Mottola, S., & Mueller, M. 2007, Icarus, 190, 236
Delbo', M., Libourel, G., Wilkerson, J., et al. 2014, Nature, 508, 233
Delbo', M., Mueller, M., Emery, J., Rozitis, B., & Capria, M. T. 2015, in Asteroids IV, ed. P. Michel, F. E. DeMeo, & W. F. Bottke (The University of Arizona Press), 107–128
Dundon, L. 2005, Master's thesis, University of Hawaii
Ďurech, J., Hanuš, J., Oszkiewicz, D., & Vančo, R. 2016, A&A, 587, A48
Ďurech, J., Sidorin, V., & Kaasalainen, M. 2010, A&A, 513, A46
Emery, J. P., Fernández, Y. R., Kelley, M. S. P., et al. 2014, Icarus, 234, 17
Emery, J. P., Sprague, A. L., Witteborn, F. C., et al. 1998, Icarus, 136, 104
Galád, A., Pravec, P., Gajdoš, Š., Kornoš, L., & Világi, J. 2007, Earth Moon and Planets, 101, 17
Galushina, T. Y., Ryabova, G. O., & Skripnichenko, P. V. 2015, Planet. Space Sci., 118, 296
Green, S. F., Meadows, A. J., & Davies, J. K. 1985, MNRAS, 214, 29P
Gustafson, B. A. S. 1989, A&A, 225, 533
Hanuš, J., Delbo', M., Ďurech, J., & Alí-Lagoa, V. 2015, Icarus, 256, 101
Hanuš, J., Ďurech, J., Brož, M., et al. 2011, A&A, 530, A134
Hiroi, T., Zolensky, M. E., Pieters, C. M., & Lipschutz, M. E. 1996, Meteoritics and Planetary Science, 31, 321
Houck, J. R., Roellig, T. L., van Cleve, J., et al. 2004, ApJS, 154, 18
Ishihara, D., Onaka, T., Kataza, H., et al. 2010, A&A, 514, A1
Jenniskens, P. 1994, A&A, 287, 990
Jenniskens, P. 2006, Meteor Showers and their Parent Comets (Cambridge University Press)
Jewitt, D., Hsieh, H., & Agarwal, J. 2015, in Asteroids IV, ed. P. Michel, F. E. DeMeo, & W. F. Bottke (The University of Arizona Press), 221–242
Jewitt, D. & Li, J. 2010, AJ, 140, 1519
Jewitt, D., Li, J., & Agarwal, J. 2013, ApJ, 771, L36
Kaasalainen, M. & Torppa, J. 2001, Icarus, 153, 24
Kaasalainen, M., Torppa, J., & Muinonen, K. 2001, Icarus, 153, 37
Kasuga, T. & Jewitt, D. 2008, AJ, 136, 881
Kinoshita, D., Ohtsuka, K., Sekiguchi, T., et al. 2007, A&A, 466, 1153
Krugly, Y. N., Belskaya, I. N., Shevchenko, V. G., et al. 2002, Icarus, 158, 294
Lagerros, J. S. V. 1996, A&A, 310, 1011
Lagerros, J. S. V. 1997, A&A, 325, 1226
Lagerros, J. S. V. 1998, A&A, 332, 1123
Landolt, A. U. 1992, AJ, 104, 340
Li, J. & Jewitt, D. 2013, AJ, 145, 154
Licandro, J., Campins, H., Mothé-Diniz, T., Pinilla-Alonso, N., & de León, J. 2007, A&A, 461, 751
Madiedo, J. M., Trigo-Rodríguez, J. M., Castro-Tirado, A. J., Ortiz, J. L., & Cabrera-Caño, J. 2013, MNRAS, 436, 2818
Müller, T. G., Hasegawa, S., & Usui, F. 2014, PASJ, 66, 52
Ohtsuka, K., Arakida, H., Ito, T., Yoshikawa, M., & Asher, D. J. 2008, Meteoritics and Planetary Science Supplement, 43, 5055
Ohtsuka, K., Nakato, A., Nakamura, T., et al. 2009, PASJ, 61, 1375
Ohtsuka, K., Sekiguchi, T., Kinoshita, D., et al. 2006, A&A, 450, L25
Opeil, C. P., Consolmagno, G. J., & Britt, D. T. 2010, Icarus, 208, 449
Ostro, S. J., Margot, J.-L., Benner, L. A. M., et al. 2006, Science, 314, 1276
Pravec, P., Harris, A. W., Kušnirák, P., Galád, A., & Hornoch, K. 2012, Icarus, 221, 365
Pravec, P., Vokrouhlický, D., Polishook, D., et al. 2010, Nature, 466, 1085
Pravec, P., Wolf, M., & Šarounová, L. 1998, Icarus, 136, 124
Rozitis, B., Duddy, S. R., Green, S. F., & Lowry, S. C. 2013, A&A, 555, A20
Rozitis, B. & Green, S. F. 2014, A&A, 568, A43
Rozitis, B., MacLennan, E., & Emery, J. P. 2014, Nature, 512, 174
Ryabova, G. O. 2007, MNRAS, 375, 1371
Sato, K., Miyamoto, M., & Zolensky, M. E. 1997, Meteoritics and Planetary Science, 32
Skiff, B. A., Buie, M. W., & Bowell, E. 1996, in Bulletin of the American Astronomical Society, Vol. 28, AAS/Division for Planetary Sciences Meeting Abstracts #28, 1104
Spencer, J. R. 1990, Icarus, 83, 27
Spencer, J. R., Lebofsky, L. A., & Sykes, M. V. 1989, Icarus, 78, 337
Tedesco, E. F., Noah, P. V., Noah, M., & Price, S. D. 2002, Astronomical Journal, 123, 1056
Tedesco, E. F., Noah, P. V., Noah, M., & Price, S. D. 2004, NASA Planetary Data System, 12
Usui, F., Kasuga, T., Hasegawa, S., et al. 2013, ApJ, 762, 56
Usui, F., Kuroda, D., Müller, T. G., et al. 2011, PASJ, 63, 1117
Vokrouhlický, D., Bottke, W. F., Chesley, S. R., Scheeres, D. J., & Statler, T. S. 2015, in Asteroids IV, ed. P. Michel, F. E. DeMeo, & W. F. Bottke (The University of Arizona Press), 509–531
Vokrouhlický, D., Nesvorný, D., & Bottke, W. F. 2003, Nature, 425, 147
Vokrouhlický, D., Nesvorný, D., & Bottke, W. F. 2006, Icarus, 184, 1
Vraštil, J. & Vokrouhlický, D. 2015, A&A, 579, A14
Warner, B. D. 2006, A Practical Guide to Lightcurve Photometry and Analysis (Springer)
Warner, B. D. 2015, Minor Planet Bulletin, 42, 115
Williams, I. P. & Wu, Z. 1993, MNRAS, 262, 231
Wisniewski, W. Z., Michałowski, T. M., Harris, A. W., & McMillan, R. S. 1997, Icarus, 126, 395
Yanagisawa, M., Ikegami, H., Ishida, M., et al. 2008, Meteoritics and Planetary Science Supplement, 43, 5169